Supporting Information

Scalable, Thermally Stabilized MOF–Graphene Fibers with Hierarchical Porosity for High-Performance Energy Storage Devices

Narges Nobakht[a,b*], Mohammad Hosseini[a], Seyyed Ahmad Etghani[a,c], Mohamad Ali Sanjari Shahrezaei[a], Ali Sajedi-Moghaddam[a,*], Seyed Hamed Aboutalebi[a,d*]

[a] Condensed Matter National Laboratory, Institute for Research in Fundamental Sciences, Tehran, 19395-5531, Iran.

[b] BattScout Company, London Road, Bishopdown, Salisbury, SP1 3, England, United Kingdom.

[c] School of Biological Sciences, Institute for Research in Fundamental Sciences, Tehran, 19395-5746, Iran.

[d] School of Quantum Physics & Matter, Institute for Research in Fundamental Sciences, Tehran, 19395-5531, Iran.

[*]Corresponding Authors:

Email Addresses:

nargesnobakht@ipm.ir (N. Nobakht)

a.sajedi@ipm.ir (A. Sajedi-Moghaddam)

hamedaboutalebi@ipm.ir (S. H. Aboutalebi)

Figure S1. Digital photograph of the synthesized PM powder, showing its characteristic blue color.

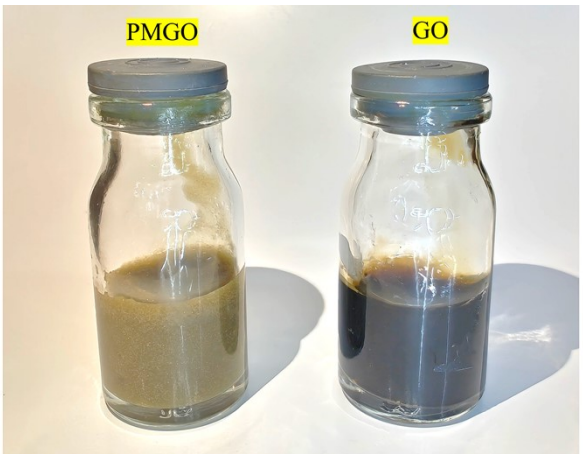

Figure S2. Digital photograph of PMGO and GO dispersions in aqueous solution. The PMGO dispersion appears light brownish due to the incorporation of PM into the GO matrix, while the GO dispersion retains its characteristic dark brown-to-black color.

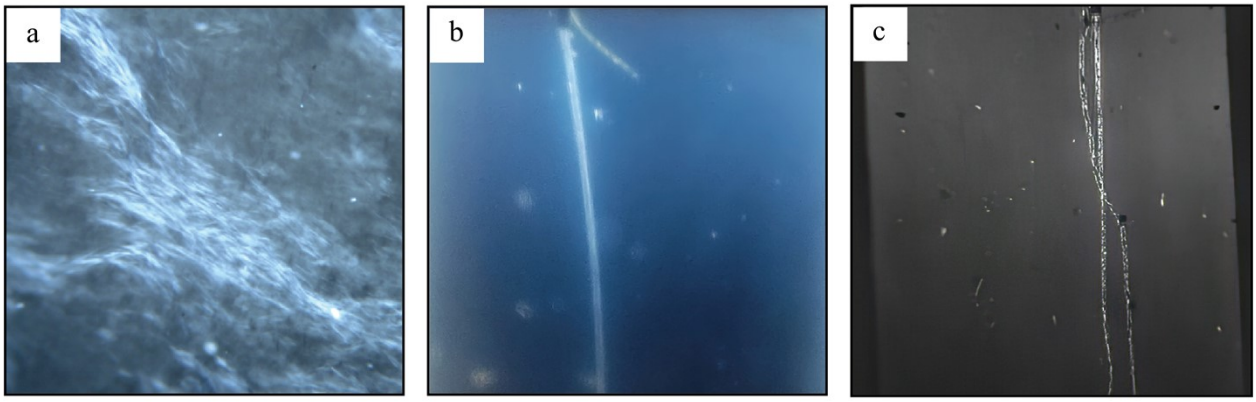

Figure S3. (a) Liquid crystalline GO and (b) PMGO dispersions in water. The introduction of PM into liquid crystalline dispersions of GO did not disrupt the liquid crystallinity of the final dispersion, ensuring effective mixing and the formation of a homogeneous liquid crystal dispersion. (c) The resulting PMGO liquid crystal dispersion was utilized in the fabrication of hybrid composites through the wet-spinning method, with isopropanol employed as the coagulation bath.

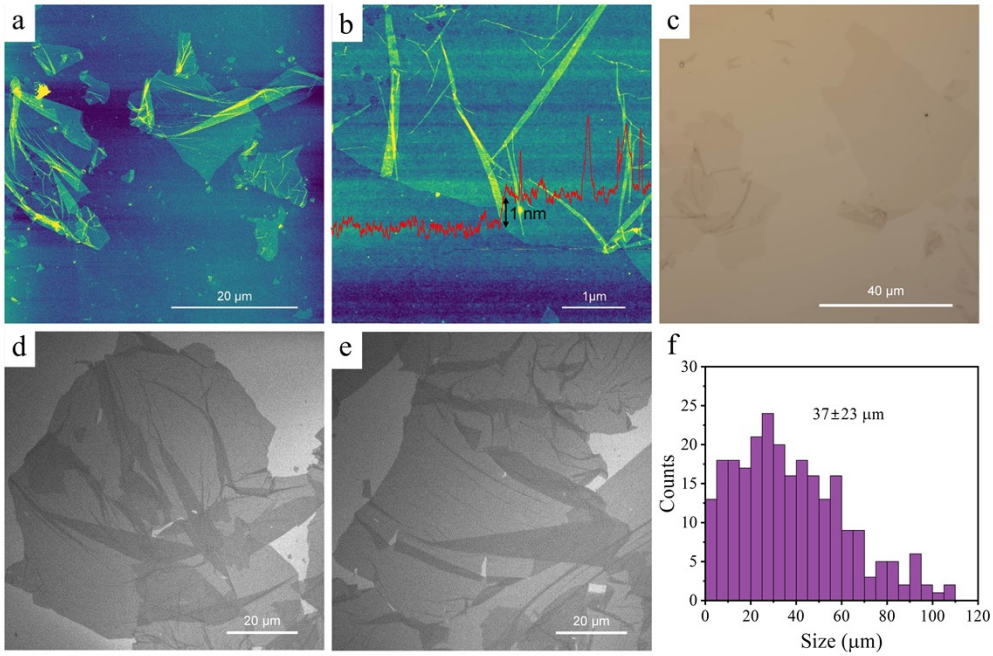

Figure S4. (a, b) AFM images of exfoliated GO sheets. The height analysis confirms exfoliation down to a monolayer. (c) OM and (d, e) FESEM images of exfoliated GO. The distinct contrast between GO sheets and the silicon substrate in both techniques confirm the predominance of monolayer structures. (f) Lateral size distribution of GO sheets derived from combined AFM, OM, and FESEM analyses.

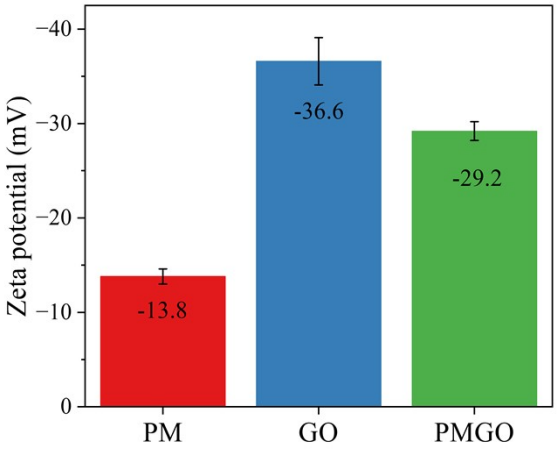

Figure S5. Zeta potential measurements of as-prepared PM, GO, and PMGO dispersions. The pristine PM dispersion shows limited colloidal stability, consistent with the poor aqueous stability of its parent MOF (Cu-BTC). In contrast, incorporation of GO enhances electrostatic repulsion and improves dispersion stability, indicating increased structural integrity and shelf-life of the PMGO hybrid system.

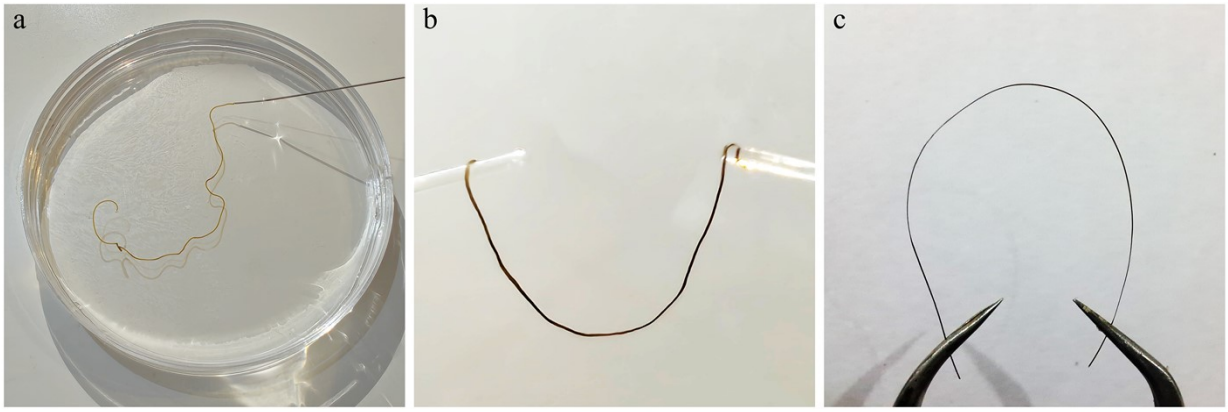

Figure S6. Photographs illustrating the fabrication and flexibility of MPGO fibers: (a) wet spinning of MPGO fiber into isopropanol medium; (b) as-spun wet flexible MPGO fiber; (c) dried flexible MPGO fiber demonstrating excellent mechanical flexibility.

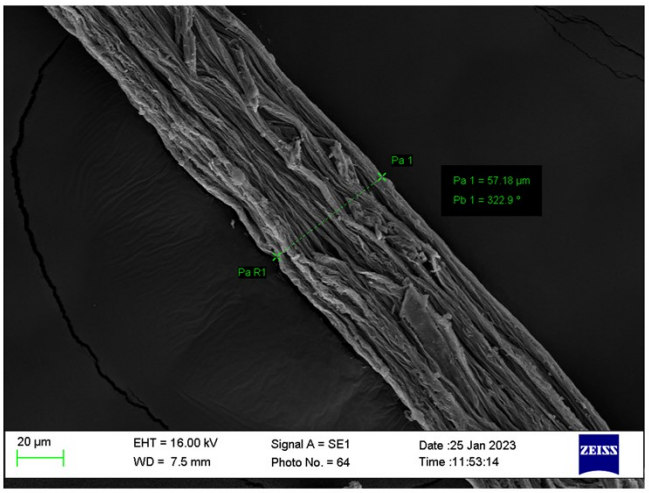

Figure S7. Representative SEM image of a single printed PMGO fiber on the substrate, showing its directionally aligned and exfoliated architecture across the fiber diameter. The observed ordered morphology is characteristic of shear-induced alignment during the printing process.

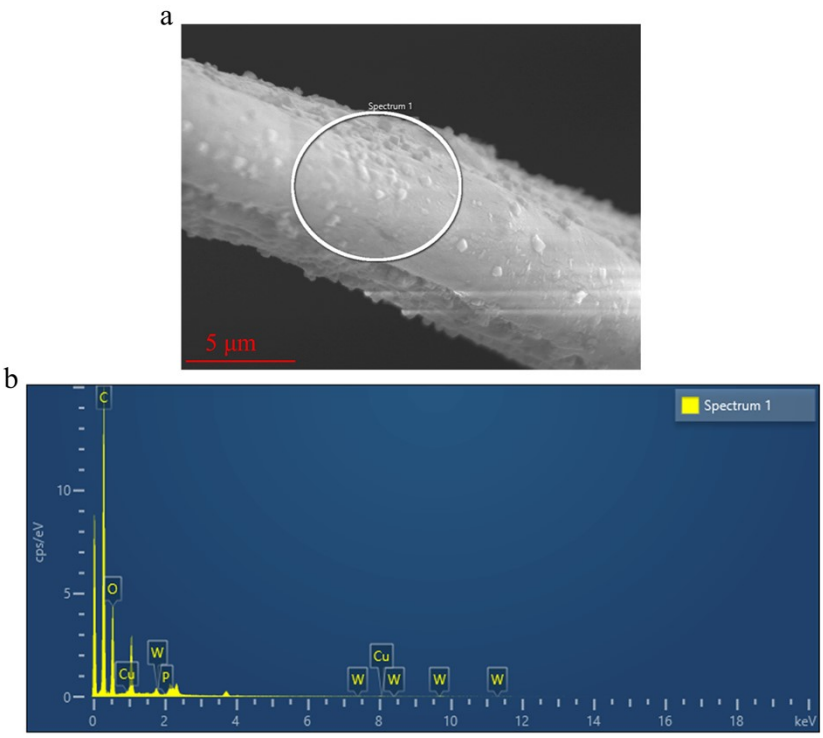

Figure S8. (a) SEM image of the PMrGO hybrid structure, showing surface morphology after thermal reduction. (b) Corresponding EDS spectrum confirming the presence of key elements including copper (Cu), tungsten (W), phosphorus (P), oxygen (O), and carbon (C), attributed to the Cu-BTC framework, polyoxometalate (HPW), and rGO matrix.

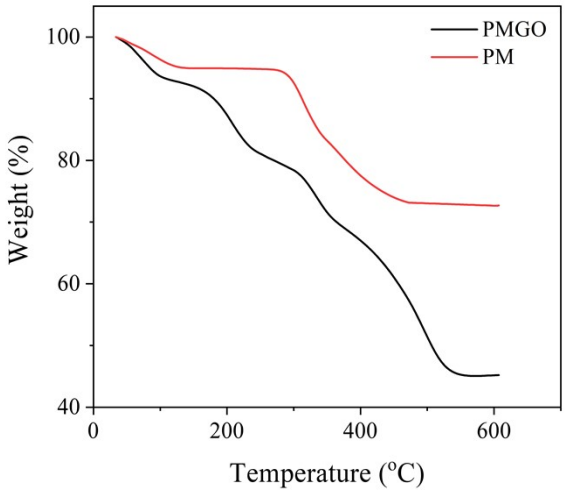

Figure S9. TGA profiles of pristine PM and PMGO recorded under ambient air. Pristine PM exhibits higher thermal stability, retaining over 80% of its weight at 300 °C. The PMGO hybrid shows characteristic weight loss associated with moisture desorption and partial thermal reduction of GO, indicating slightly reduced stability compared to PM alone.

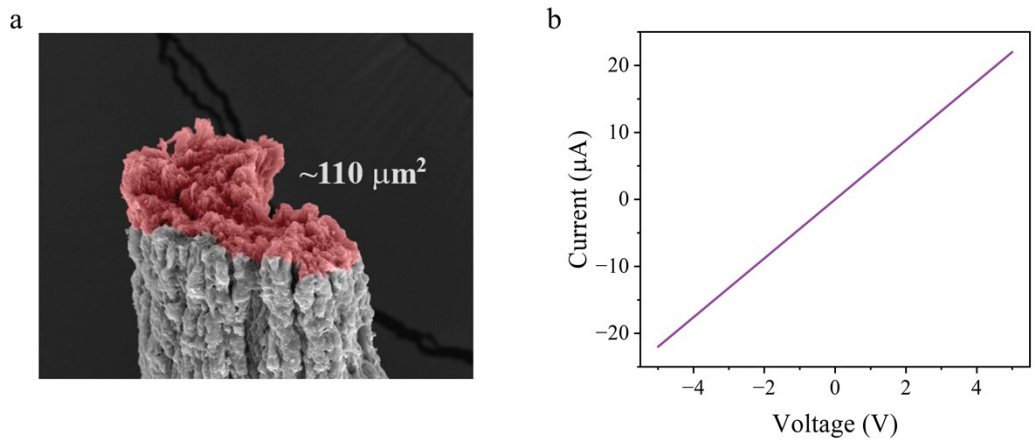

Figure S10. (a) FESEM image of an individual as-prepared PMrGO fiber used for electrical characterization, showing a measured probe contact area of ~110 μm^2. (b) Corresponding current–voltage (I–V) curve, displaying a linear response characteristic of ohmic behavior. The fiber exhibits a native electrical conductivity of ~5600 S m^{-1}, nearly twice that of pure rGO fibers, attributed to improved charge transport enabled by thermal reduction and the presence of PM.

Table S1. Comparison of Young's modulus values for GO-, rGO-, and PMrGO-based fibers prepared in this study and from previous reports. The table highlights the influence of coagulation conditions and fiber composition on mechanical performance. PMrGO fibers fabricated in this work exhibit the highest modulus, demonstrating significant enhancement over both pristine and previously reported rGO-based fibers.

Production condition	Young's Modulus (GPa)	Reference
PMrGO fibers coagulated in isopropanol bath	42.64±2.0	This work
rGO fibers coagulated in isopropanol bath	24.25±3.5	This work
GO fibers coagulated in acetone bath	20.5±2.75	1
rGO fibers coagulated in acetone bath	10.13±2.25	1
GO fibers coagulated by chitosan	22.6±1.9	2
GO fibers coagulated by calcium chloride	20.1±2.1	2

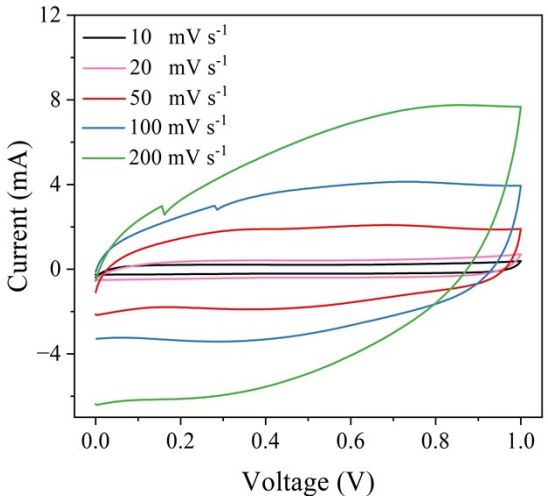

Figure S11. CV profiles of PrGO electrode recorded at scan rates from 10 to 200 mV s^{-1}. The quasi-rectangular shape indicates dominant EDLC behavior, with slight distortion suggesting minor pseudocapacitive contributions from the redox-active HPW species.

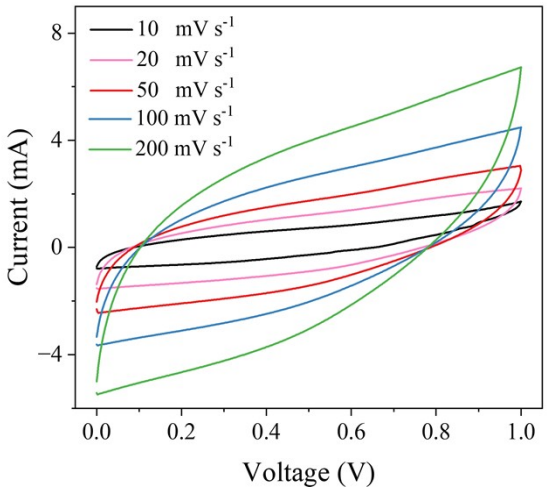

Figure S12. CV profiles of PMrGO composite electrodes recorded at scan rates ranging from 10 to 200 mV s^{-1}. The distorted CV shape reflects significant pseudocapacitive behavior arising from the redox-active Cu^{2+} centers in the MOF and the hierarchical porous structure. Compared to fiber-based PMrGO architectures, the composite form exhibits lower current response, likely due to reduced structural alignment and interfacial conductivity.

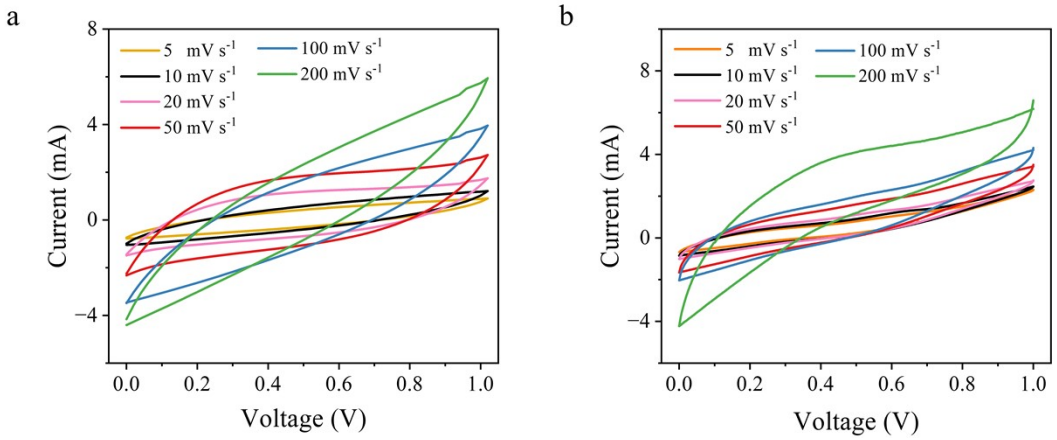

Figure S13. CV profiles of PMrGO hybrid fiber electrodes with varying PM content, recorded at scan rates from 10 to 200 mV s^{-1}: (a) 25 wt% PM and (b) 75 wt% PM. Increased PM loading leads to more pronounced pseudocapacitive features in the CV curves, reflecting greater redox contribution from the Cu-BTC framework.

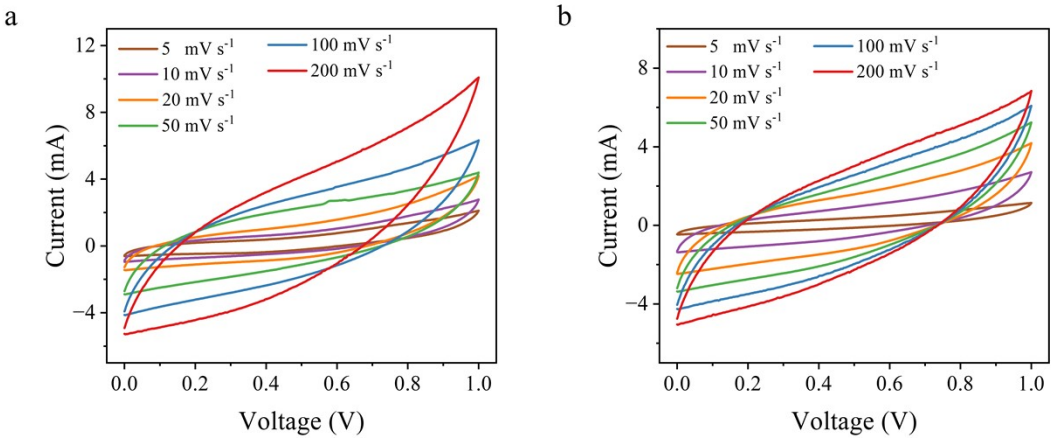

Figure S14. CV profiles of PMrGO hybrid fiber electrodes recorded at scan rates from 10 to 200 mV s^{-1} in (a) 1 M H_2SO_4 and (b) 1 M KOH aqueous electrolytes. Both electrolytes result in reduced current response and less pronounced pseudocapacitive features compared to neutral conditions, likely due to the destabilizing effect of protons (H^+) and hydroxide ions (OH^-) on the metal–ligand coordination environment within the Cu-BTC framework.

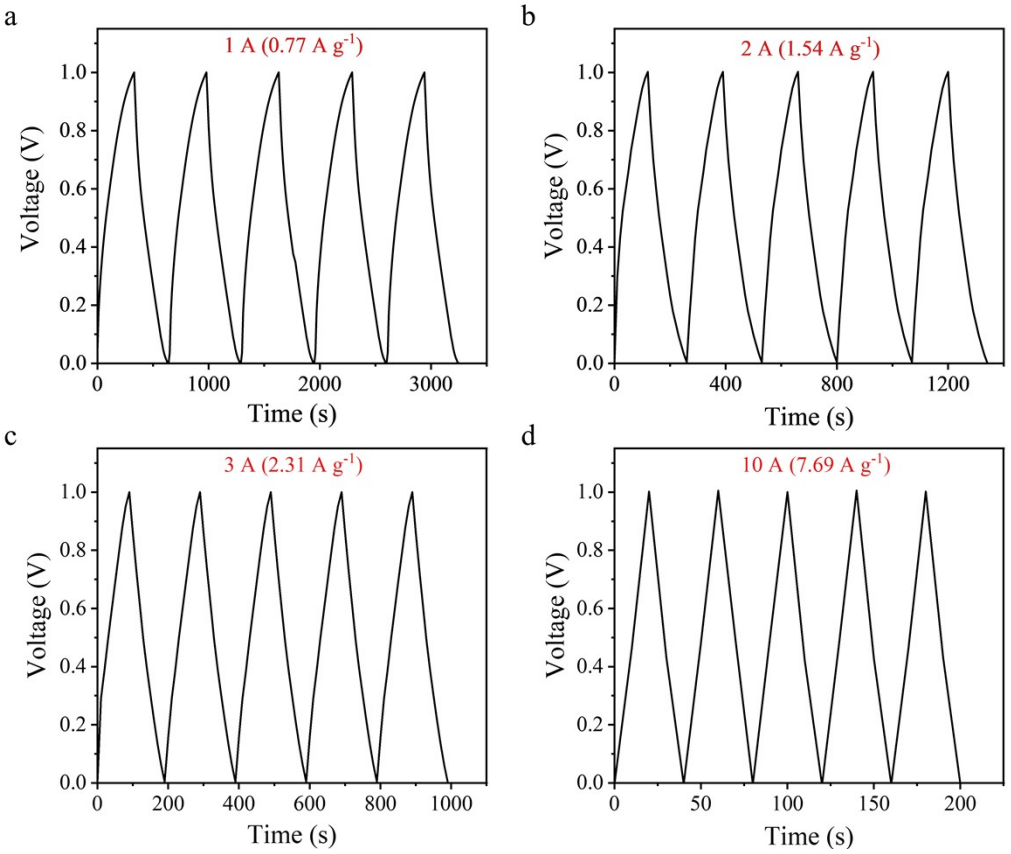

Figure S15. GCD curves of PMrGO hybrid fiber electrodes recorded over 5 cycles in 1 M NaCl at current densities of (a) 0.77 A g^{-1}, (b) 1.54 A g^{-1}, (c) 2.31 A g^{-1}, and (d) 7.69 A g^{-1}. Across all current densities, the curves exhibit no observable IR drop, indicating excellent electrical conductivity and strong interfacial contact between the electrode and current collector. These characteristics confirm the high-rate capability of the as-printed PMrGO architecture.

Table S2. Energy storage performance metrics of PMrGO hybrid fiber electrodes, derived from galvanostatic charge–discharge (GCD) measurements in 1 M NaCl. Reported parameters include I_G (gravimetric current density, A g^{-1}), C_G (gravimetric capacitance, F g^{-1}), E_G (gravimetric energy density, Wh kg^{-1}), P_G (gravimetric power density, kW kg^{-1}), I_A (areal current density, mA cm^{-2}), C_A (areal capacitance, mF cm^{-2}), E_A (areal energy density, μWh cm^{-2}), and P_A (areal power density, mW cm^{-2}).

I_G	C_G	E_G	P_G	I_A	C_A	E_A	P_A
0.77	476.92	16.56	0.19	0.69	430.56	29.90	0.35
1.54	430.77	14.96	0.38	1.39	388.89	27.01	0.69
2.31	461.54	16.03	0.58	2.08	416.67	28.94	1.04
6.15	369.23	12.82	1.54	5.56	333.33	23.15	2.78
7.69	307.69	10.68	1.92	6.94	277.78	19.29	3.47

Table S3. Comparative electrochemical performance of PMrGO SCs developed in this work versus previously reported graphene-based hybrid fiber SCs, all tested in two-electrode configurations. The table summarizes the electrolyte used and key performance parameters: V (voltage window, V), C_A (areal capacitance, mF cm^{-2}), E_A (maximum areal energy density, μWh cm^{-2}), and P_A (maximum areal power density, mW cm^{-2}).

Electrode materials	Electrolyte	V	C_A	E_A	P_A	Ref.
PMrGO	NaCl	1	430.56	29.90	3.47	This work
rGO/PEDOT:PSS	PVA/H_3PO_4	0.8	304.5	27.1	0.07	3
N-doped SiN/GF	PVA/H_2SO_4	1.0	263.6	6.29	0.3	4
PANI/GF	PVA/H_2SO_4	0.8	---	7.93	0.23	5
MoS_2/GF	PVA/H_2SO_4	0.8	189.7	14.67	0.66	6
CNT/MXene/GF	PVA/H_2SO_4	0.8	237	5.3	0.02	7
CuS|P-CuGFs//AC-GFs	PVA/KOH	1.5	---	15.3	6.37	8
rGO/MXene	PVA/H_2SO_4	0.8	550.96	12	8.8	9
NS-GF@RuO_2	PVA/H_2SO_4	1.0	~20	1.02	0.13	10

Note: N-doped SiN/GF denotes nitrogen-doped siloxene/graphene fibers. CuS|P-CuGFs//AC-GFs is an asymmetric SC composed of copper phosphosulfide nanosheets (CuS|P NSs) grown in situ on copper-coated graphene fibers (CuS|P-CuGFs) as the positive electrode and activated carbon-coated graphene fibers (AC-GFs) as the negative electrode. NS-GF@RuO_2 refers to nitrogen and sulfur co-doped graphene fibers decorated with RuO_2 nanoparticles. All other materials are named according to their composite components and are detailed in their respective references.

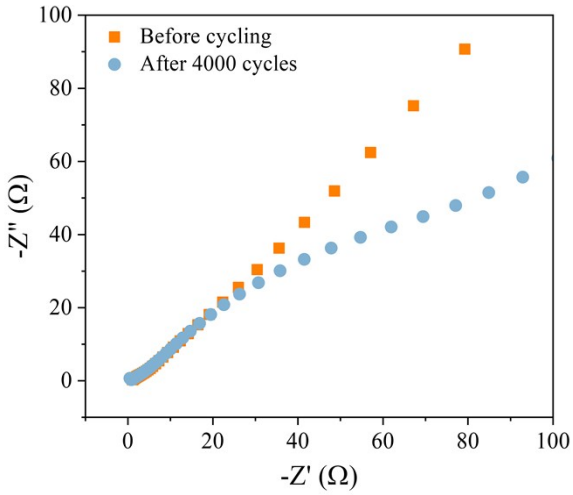

Figure S16. Nyquist plots of PMrGO SCs recorded before and after 4000 charge–discharge cycles. Minimal changes in the high-frequency region indicate stable equivalent series resistance (ESR), while the slight shift in the low-frequency region suggests increased resistive contributions, likely due to structural or interfacial degradation over extended cycling.

References:

1 S. H. Aboutalebi, R. Jalili, D. Esrafilzadeh, M. Salari, Z. Gholamvand, S. Aminorroaya Yamini, K. Konstantinov, R. L. Shepherd, J. Chen, S. E. Moulton, P. C. Innis, A. I. Minett, J. M. Razal and G. G. Wallace, *ACS Nano*, 2014, **8**, 2456–2466.

2 R. Jalili, S. H. Aboutalebi, D. Esrafilzadeh, R. L. Shepherd, J. Chen, S. Aminorroaya-Yamini, K. Konstantinov, A. I. Minett, J. M. Razal and G. G. Wallace, *Adv. Funct. Mater.*, 2013, **23**, 5345–5354.

3 G. Qu, J. Cheng, X. Li, D. Yuan, P. Chen, X. Chen, B. Wang and H. Peng, *Adv. Mater.*, 2016, **28**, 3646–3652.

4 B. Bai, L. Qiu, Y. Yuan, L. Song, J. Xiong and P. Du, *J. Energy Storage*, 2023, **63**, 106984.

5 X. Zheng, L. Yao, Y. Qiu, S. Wang and K. Zhang, *ACS Appl. Energy Mater.*, 2019, **2**, 4335–4344.

6 M. Tang, Y. Wu, J. Yang and Y. Xue, *J. Alloys Compd.*, 2020, **828**, 153622.

7 R. Xiang, J. Zhang, X. Yang, Y. Liu, C. Lu, X. Wang and K. Zhang, *ACS Appl. Energy Mater.*, 2022, **5**, 13212–13221.

8 B. Bai, J. Shui, Y. Wang, Z. Su, L. Qiu and P. Du, *ACS Appl. Nano Mater.*, 2024, **7**, 12387–12398.

9 N. He, S. Patil, J. Qu, J. Liao, F. Zhao and W. Gao, *ACS Appl. Energy Mater.*, 2020, **3**, 2949–2958.

10 S. H. Noh, H. B. Lee, K. S. Lee, H. Lee and T. H. Han, *ACS Appl. Mater. Interfaces*, 2022, **14**, 29867–29877.